



Integrated textural and geochemical analysis of igneous zircon by atom probe tomography

Michelle L. Foley^{1,2} · Elias M. Bloch^{1,3} · Stephan S.A. Gerstl⁴ · Benita Putlitz¹ · Lukas P. Baumgartner¹

Received: 1 June 2024 / Accepted: 19 August 2024 / Published online: 30 August 2024
© The Author(s) 2024

Abstract

Mechanisms relating to growth and/or compositional modification of zircon occur at the atomic scale. For felsic igneous systems, processes responsible for growth patterns in zircon have previously remained elusive as the volume of material needed to analyze these compositional features using traditional in-situ methods is considerably larger than the typical sub-micron scale distribution of trace elements. To illuminate some of these driving forces, we characterize and quantify minor and trace element concentrations in igneous zircon grains by combining methods of cathodoluminescence (CL) imaging, electron microprobe microanalysis (EMPA) elemental maps for Hf, Y, Yb and U or Th, and atom probe tomography (APT). We focus on igneous zircon from the Chon Aike Silicic Large Igneous Province (Patagonia) that provide novel insights into (1) dissolution and re-crystallization during crustal anatexis, (2) crystallization to produce oscillatory zonation patterns that are typical of igneous zircons, and (3) the incorporation of trace element impurities (e.g., P, Be, and Al) at the nanoscale. Significantly, these APT volumes provide nanoscale sampling of boundaries between oscillatory growth zones in an igneous zircon to reveal compositional zoning of Y and, to a lesser extent P, which appear as high-angle, planar features. These concentration boundaries measured on the order of 10 to 12 nm are difficult to reconcile with proposed mechanisms for generating fine-scaled oscillations. Lastly, we fit diffusional profiles to measured Y concentrations to provide an estimate on the maximum timescales of zircon growth prior to eruption, as a function of the temperature at which diffusion occurred. When combined with known pressure-temperature-time paths for the magmatic system considered, these extremely short diffusion profiles that are resolvable by APT provide a powerful method to constrain timescales of crystal growth.

Keywords Zircon · Atom probe tomography · Crystal growth · Oscillation · Trace elements · Crustal anatexis

Introduction

The use of zircon for many geologic applications derives from its incorporation of natural radionuclides (U, Th, and Hf) and trace elements that are indicative of the growth conditions and/or relating to reactions (Cherniak and Watson 2003; Kinny and Maas 2003), rejection of Pb, low solubility in crustal melts and fluids (Harrison and Watson 1983; Watson and Harrison 1983; Watson 1996b; Szymanowski et al. 2020), and the slow diffusivities of its constituent ions (Cherniak et al. 1997a, b; Bloch et al. 2022). The typical size of zircon (~100s of microns), together with its resistance to chemical and physical breakdown in most geological environments, make it a unique tracer of the protracted history of Earth. During crustal anatexis and/or assimilation, complete zircon dissolution is rarely reached, as is testified by the preservation of inherited zircon cores granites

Communicated by Dante Canil.

✉ Michelle L. Foley
michellefoley@arizona.edu

- ¹ Institute of Earth Sciences, University of Lausanne, UNIL-Mouline, Lausanne 1015, Switzerland
- ² Department of Geosciences, University of Arizona, Tucson, AZ 85721, USA
- ³ Lunar and Planetary Laboratory, University of Arizona, Tucson, AZ 85721, USA
- ⁴ Scientific Center for Optical and Electron Microscopy, ETH Zürich, Zürich 8093, Switzerland

and granitoids with a crustal component (e.g., Miller et al. 2007; Bea et al. 2007), and by multiple age domains from high-grade poly metamorphic rocks, including granulite facies (e.g., Möller et al. 2003; Rubatto et al. 2013; O'Brien and Miller 2014; Kunz et al. 2018). Although ideal zircon (ZrSiO_4) is stable under crustal and upper-mantle conditions, observations indicate that primary zircon is not always in equilibrium with its surrounding environment. In this study, the preservation of inherited zircon in the felsic volcanic rocks from the Patagonian Chon Aike Silicic Large Igneous Province provide an opportunity to study the dynamic crystallization environment for detrital zircon grains that were incorporated into felsic melts generated during crustal anatexis of metasedimentary lithologies (Foley et al. 2023a, b).

Atom Probe Tomography (APT) is a 3-dimensional analytical technique that provides the chemical composition and position of each detected ion within a small volume of analyzed material (e.g., $<0.02 \mu\text{m}^3$), which is used to visualize and quantify chemical variations at sub-micrometer scales (Valley et al. 2014, 2015; Saxey et al. 2018; Reddy et al. 2020). Recent APT studies on zircon have highlighted the importance of this technique for understanding elemental and isotopic distribution at the nanometer scale, in terms of providing information about crystallization and thermal histories, as well as for identifying mechanisms of mineral reaction and exchange (e.g., Fougereuse et al. 2024). Studies on deformed (e.g., Piazzolo et al. 2016; Reddy et al. 2016; La Fontaine et al. 2017) and/or metamorphosed zircon (e.g., Peterman et al. 2019; Taylor et al. 2023) have demonstrated the potential for trace element mobility and/or clustering when grains are subjected to sustained high-temperature and pressure stresses. Furthermore, identifying the mechanisms of intracrystalline Pb mobility in zircon has been significant for understanding discordance in the U-Pb system (e.g., Valley et al. 2014; Valley et al. 2015; Peterman et al. 2016).

Nanoscale research directed at characterizing processes related to dissolution and growth of igneous zircon has received little attention. Here, we combine cathodoluminescence (CL) imaging and electron microprobe analysis (EMPA) trace element maps that provide information about the microscopic trace element distribution within the zircon with APT to trace the distribution of elements and characterize the nanoscale structure and chemistry of complex core-rim interface domains between an inherited core and the younger autocrystic overgrowth. We targeted inherited zircon cores to test for compositional modifications and/or alteration due to thermal perturbations during crustal anatexis. Within these grains, it is common to observe variable dissolution textures preserved within zircon crystals; therefore, APT of such crystals may reveal compositional information pertaining to the melt both prior to and after dissolution within these overgrowth domains.

Lastly, oscillatory growth zones are observed in most igneous zircon (Hoskins and Schaltegger 2003), indicating that there are common driving forces controlling the trace element distribution during zircon growth from a felsic melt. However, constraining the processes responsible for growth patterns has remained elusive, as the volume of material needed to analyze these compositional features is considerably larger than the typical sub-micron scale distribution of trace elements. Here, we analyze portions of an autocrystic zircon domain characterized by fine-scaled oscillatory growth zones by APT that reveal near stepwise concentration gradients between growth zones on the order of nanometers. We also use Y concentration profiles and diffusion modeling to estimate the timescale of autocrystic zircon growth prior to eruption.

Geologic background and prior sample characterization

The Chon Aike Silicic Large Igneous Province (CASP) consists of an estimated 235,000 km³ of predominately felsic volcanic rocks distributed throughout Patagonia and the Antarctic Peninsula (Pankhurst et al. 1998) (Fig. 1). Geochronological studies indicate that volcanism occurred over 45 Myr, incipient to the break-up of the Gondwanan supercontinent throughout the Jurassic (Pankhurst et al. 2000; Foley et al. 2024). Field, geochemical, and isotope evidence support a crustal origin for the felsic magmas of the CASP (Gust et al. 1989; Pankhurst and Rapela 1995; Pankhurst et al. 1998; Riley et al. 2001; Seitz et al. 2018; Foley et al. 2023a, b). The El Quemado Complex (EQC) is the youngest eruptive episode of the CASP at ca. 148 to 152 Ma and is characterized by rhyolitic and dacitic ignimbrites. Elevated $\delta^{18}\text{O}$ values measured in quartz and zircon and non-radiogenic zircon Hf isotope values require $>70\%$ of the EQC magmas to be derived from partial melting of the local metasedimentary basement rocks (Foley et al. 2023a, b). Further evidence for metasediments as the source of the EQC magmas is supported by the preservation of inherited zircon cores that were derived from incorporation of detrital zircon grains during anatexis (Fig. 2).

We focus on a dacitic ignimbrite from the El Chaltén region of Argentina, which hosted numerous inherited zircon cores (Fig. 2). The zircon of ignimbrite sample LCMF14 were previously analyzed for U-Pb, initial ϵ_{Hf} , and trace element concentrations by laser ablation-inductively coupled-mass spectrometry (LA-ICP-MS) methods and $\delta^{18}\text{O}$ composition by secondary ion mass spectrometry (SIMS; Foley et al. 2023a). The LCMF14 zircon population has ^{18}O -enriched compositions ranging from 8.5 to 10.0‰ and negative initial ϵ_{Hf} values of -4.7 to -9.8. Trace element

Fig. 1 Simplified geologic map of the Chon Aike Silicic Large Igneous Province in southern Patagonia of South America, with felsic volcanic outcrops illustrated in grey and mafic to intermediate outcrops in black. Zircon grains from this study sourced are from a dacitic ignimbrite from the El Quemado Complex sampled in El Chaltén, Argentina (green star)

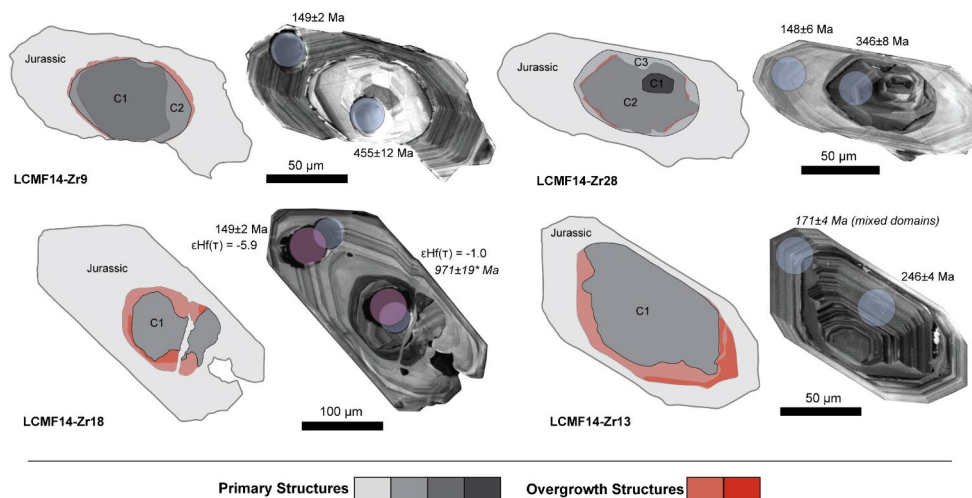
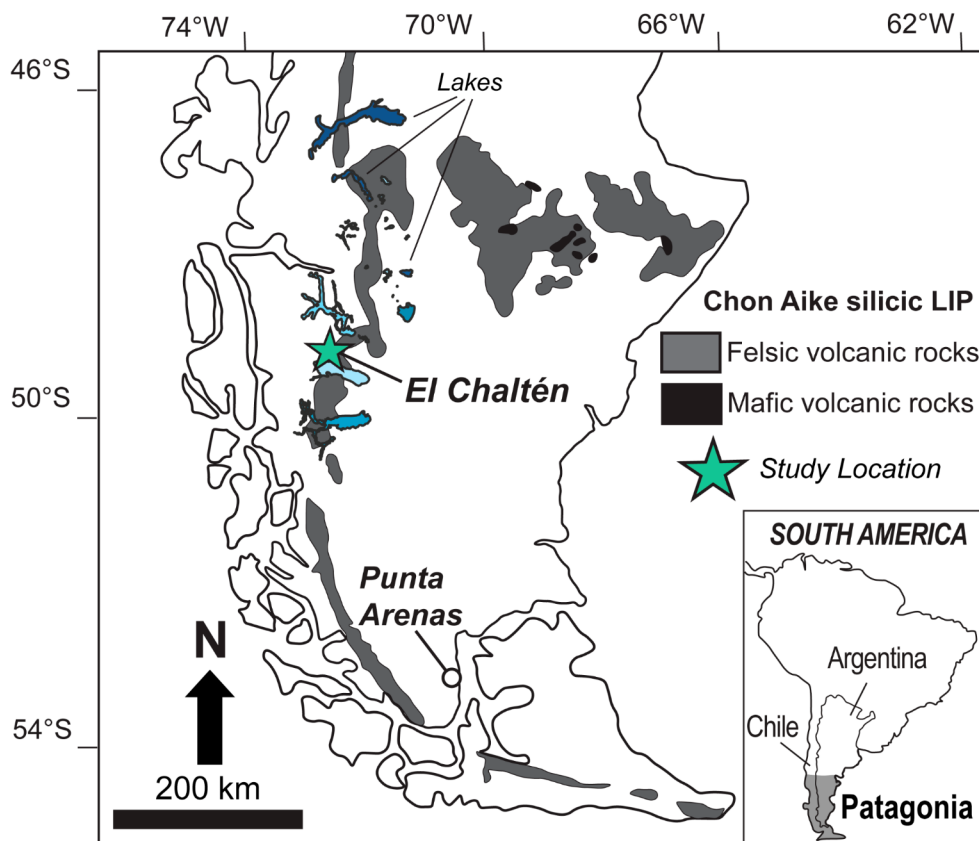


Fig. 2 Four zircon grains selected from an ignimbrite from the Los Cóndores section (LCMF14) illustrating Late Jurassic-aged magmatic zircons overgrowths with inherited zircon grains of various age. In all cases, the autocrystic domain and inherited core display CL textures of primarily oscillatory zonation are identified here as primary structures and interpreted as indicating magmatic growth. We designate

analyses of the Jurassic domains by LA-ICP-MS yield average concentrations of 10,700 ppm for Hf, 1250 ppm for Y, 375 ppm for Yb, 110 ppm for Th, and 190 ppm for U.

Inherited cores were identified based on distinct changes in cathodoluminescence (CL) textures (Fig. 2), wherein

growth events within the cores (i.e., C1, C2, C3) based on changes in Hf concentrations as observed in the EMPA elemental maps in Fig. 3. Overgrowth structures occur at the contact between the inherited and autocrystic zircon domain and are observed as irregular surfaces with typically a homogeneous CL greyscale intensity. U-Pb analyses are indicated with a blue circle and Lu-Hf analyses in purple

growth surfaces are often truncated by dissolution surfaces that are then overgrown by euhedral growth zones that exhibit oscillatory zonation. Inherited cores have a range of CL patterns from homogeneous in greyscale value to having oscillatory zonation – though they are commonly texturally

distinct from the autocrystic domains. Here, we selected four zircon grains from sample LCMF14 for trace element analysis by EMPA. In all instances, Jurassic-aged autocrystic rims precipitated onto older inherited zircon (Fig. 2) with ages that ranged from the youngest at 246 ± 4 Ma ($^{206}\text{Pb}/^{238}\text{U}$) to the oldest age of 971 ± 19 Ma ($^{207}\text{Pb}/^{206}\text{Pb}$). One grain was also previously analyzed for Hf isotope values where the Jurassic rim has a value of $-5.9 \text{ } \epsilon\text{Hf}_{(149 \text{ Ma})}$ and the inherited core has a value of $-1.0 \text{ } \epsilon\text{Hf}_{(971 \text{ Ma})}$. Two zircon grains were selected for high-resolution investigation by APT based on textures observed in CL and concordant U-Pb dates (Zr9 and Zr18; Fig. 2).

Methods

Scanning electron microscopy – cathodoluminescence imaging

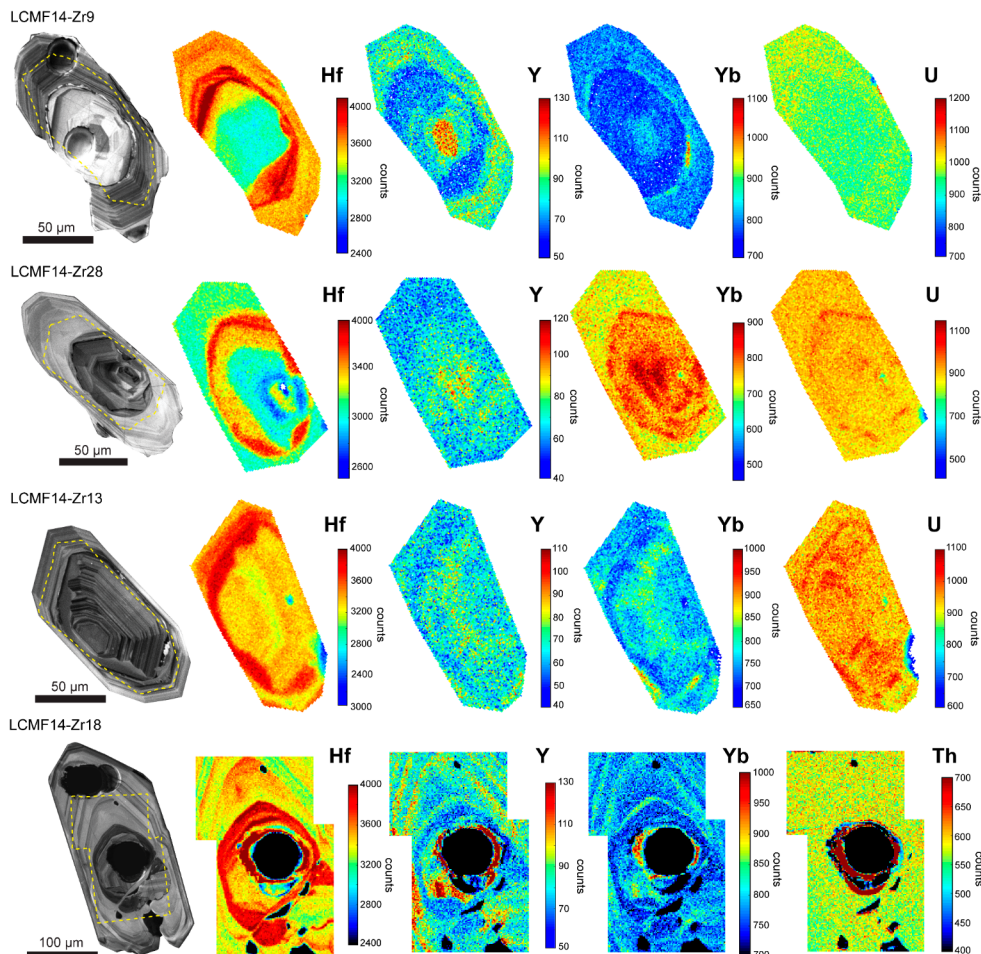
Zircon grains were imaged on a scanning electron microscope (SEM) with CL using a CamScan MV2300 SEM at the University of Lausanne (Switzerland). CL images were

acquired using an accelerating voltage of 10 kV and absorption current ranging from ~ 400 to 700 pA .

Electron microprobe analysis

EMPA elemental maps of four zircon grains were obtained using a JEOL JXA-8530 F Plus Hyperprobe equipped with a Field Emission Gun (FEG) at the University of Lausanne, Switzerland. Three of the FEG-EMPA elemental maps were analyzed for Na (TAPL, $K\alpha$), Hf (LIFL, $L\alpha$), Y (PETJ, $L\alpha$), Yb (LIFL, $L\alpha\text{-MR}$), and U (PETL- $M\beta\text{-MR}$). The fourth map was analyzed for concentrations of Na, Hf, Y, Yb, and Th (PETL, $M\alpha$). Elemental maps were performed using an accelerating voltage of 25 kV, beam current of $4.5 \times 10^{-7} \text{ A}$, and dwell time of 300 ms per pixel. The pixel size was set to $1 \times 1 \text{ } \mu\text{m}^2$. Final elemental maps ranged in area from 7500 to $21,000 \text{ } \mu\text{m}^2$ (Fig. 3). Maps for Na concentrations and an additional EMPA map are provided in the supplementary material (SF1-2).

Fig. 3 Electron Microprobe (EMPA) trace element maps of four zircon reveal distinct zoning patterns for measured concentrations of Hafnium (Hf), Yttrium (Y), Ytterbium (Yb), and Uranium (U) or Thorium (Th). Major changes in CL intensity often mirror the distribution of Hf, while variations in Y and Yb are more generally correlated to fine-scaled features within the zircon crystal. Changes in U concentrations are only observed in two zircons and correspond to the darkest CL bands (e.g., Zr28 and Zr13). The EMPA map is outlined in a yellow dashed line on the CL image; pixel dimensions are $1 \times 1 \text{ } \mu\text{m}$



Focused Ion Beam – scanning electron microscopy

Atom probe specimens (M#) were prepared from three transects sampled from two zircon grains, Zr9 (L1) and Zr18 (L1 and L2; Fig. 4). In all cases, the analyzed lift-outs crossed an interface between the phenocryst, an overgrowth structure, and its inherited core.

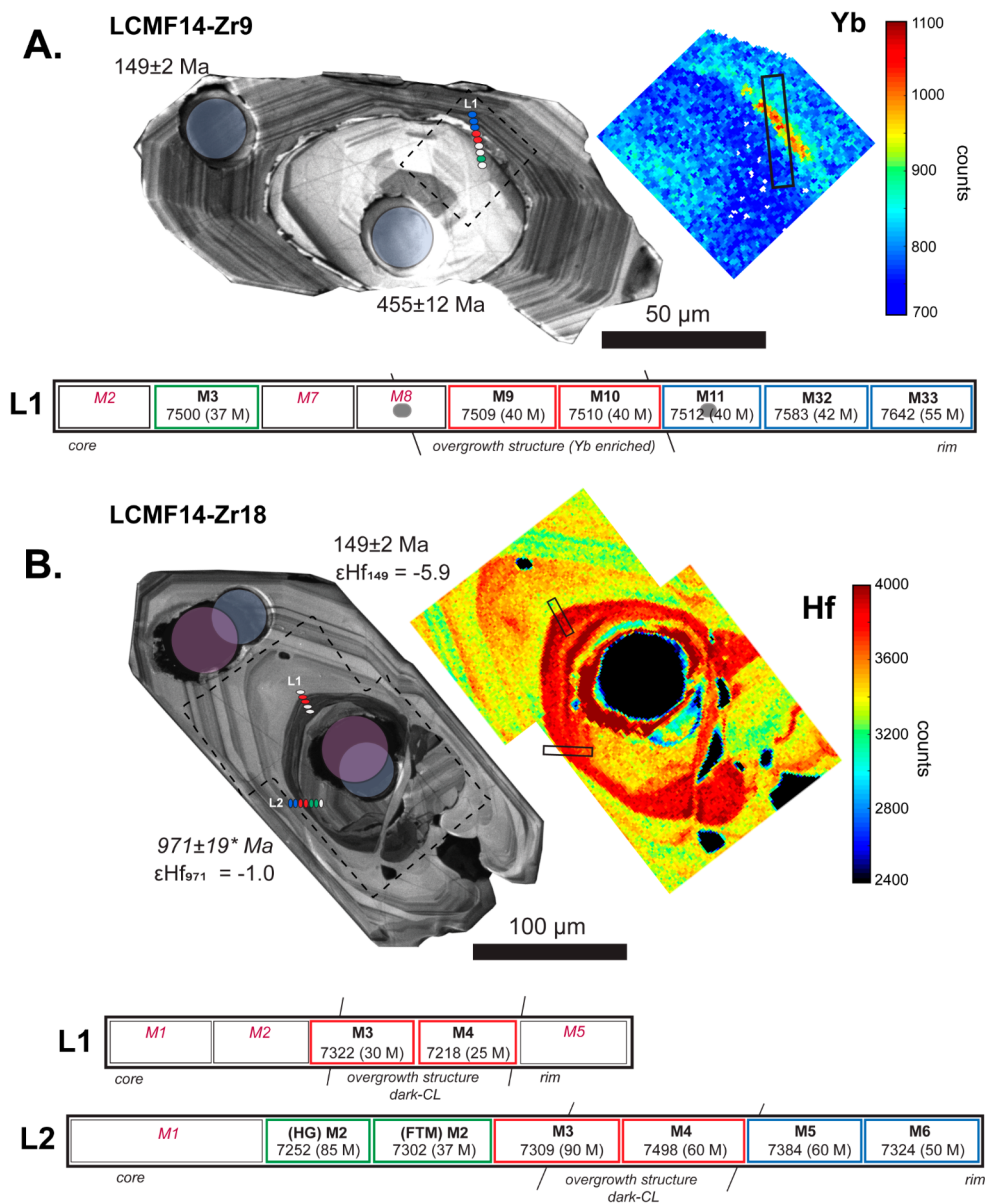
The preparation of APT specimens was performed using the FEI Helios NanoLab 600i ThermoFisher Scientific Focused Ion Beam Scanning Electron Microscopy (FIB-SEM) housed in the Scientific Center for Optical and Electron Microscopy (ScopeM) at ETH Zürich, Switzerland. The precise location for selecting specimen lift-outs was performed using the Maps 3.5 software (ThermoFisher Scientific design), where the CL image for each zircon grain was georeferenced to the FIB-SEM secondary electron (SE) image.

More detailed information pertaining to the preparation of APT specimens is available in the supplementary materials (SF3).

Atom probe tomography

Atom probe tomography data was collected at the ETH ScopeM facility using a Cameca Local Electrode Atom Probe (LEAP) 4000X-HR equipped with a laser pulsing system and a reflectron to enhance isotopic resolution. Locating the tip apex and setting the dimensions of the detector was performed in voltage mode. Final analyses were performed in laser mode, using a 355 nm-wavelength laser with a typical pulse energy of 300 pJ and 125 kHz pulse frequency to field evaporate the samples at ~50 K; additional acquisition and reconstruction parameters are given in ST1, following

Fig. 4 Two zircon grains selected for Atom Probe Tomography with locations of FIB-SEM lift-outs indicated (L1, L2). **A** Transect L1 in Zr9 is extracted across the core-rim interface at the location where Yb concentrations are enriched. **B** Two transects were taken across the core-rim interface in Zr18. Locations of APT specimens that ran successfully are indicated by filled circles (green, blue, or red) on the CL image, while white circle did not run. Colors of circles designate different portions of the zircon, including green for the inherited zircon domain, red for the overgrowth structure, and blue for the autocrystic domain. An illustration of the three transects and corresponding specimen and run names is provided below each zircon grain; lines across the transect illustration indicate the locations between major zircon domains, based on CL intensity



the guidelines of Blum et al. (2018). This pulse rate was required for the detection of masses greater than 200 Dalton (mass-to-charge-state ratio). Field stabilized zircon tips were run at target detection rates ranging from 0.3 to 0.8 ions/100 pulses (ST1). To maintain the target detection rate, the voltage was gradually increased throughout the analysis. Ions were recorded on a position-sensitive detector and the composition was determined using time-of-flight (TOF) mass spectrometry, enabling the 3-D reconstruction of the position and composition of individual atoms (isotopes and species) within the specimen with a spatial resolution of approximately 0.3 nm.

Data reconstruction and analysis was performed using IVAS (Integrated Visualization and Analysis Software) version 3.8.6 from Cameca Instruments Inc. The identification of each element and its respective isotope was conducted semi-manually (ST3). The mass resolving power for each dataset was greater than 1000 (full width half maximum) on $^{16}\text{O}_2$. The bulk composition of each APT specimen was obtained from the mass spectrum using peak deconvolution of the isotopes based on the natural isotope abundances of each isotope. The calculated standard deviation of the bulk composition value is obtained using the square root of the number of background-corrected counts. User-defined chemical isoconcentration surfaces were used to separate low and high concentration volumes and to delineate localized solute contents (i.e., enrichments) within the reconstructed data and estimate their morphology and chemical compositions; for the isosurfaces shown in text, the grid parameters include a voxel size of 1 nm^3 and delocalization of 5 nm^3 .

Results

SEM – CL Imaging

We separate our presentation of zircon crystallization textures observed in CL images between those that reflect primary structures (i.e., interpreted as uninterrupted rhythmic growth) versus overgrowth structures (i.e., interpreted as growth after dissolution; Fig. 2). The primary growth structures in the Jurassic-aged autocrystic zircon domains and its inherited core are typically observed as oscillatory zonation, with subtle variations in greyscale intensities. Inherited cores are commonly texturally distinct from the overgrowth zircon domain (Fig. 2), wherein growth surfaces are often truncated by dissolution surfaces followed by the precipitation of overgrowth structures. Overgrowth structures occur at the interface between the inherited and autocrystic zircon domains and are observed as irregular surfaces with a CL pattern that appear with a homogeneous greyscale intensity.

Within the dacitic ignimbrite sample (LCMF14), textural variability is observed for multiple zircon grains (Fig. 2), represented here by the four grains shown. Considering the four zircon grains presented here, the autocrystic domains have oscillatory zones that vary on different length scales. A subset of the zircon grains exhibit small-scale, finely spaced zones (e.g., observable resolution of $\sim 1\ \mu\text{m}$) of alternating bright and dark CL intensity (e.g., Zr9 and Zr13; Fig. 2), while other zircon grains have much wider zones (e.g., 5 to $8\ \mu\text{m}$ in Zr18 and Zr28; Fig. 2). Characteristically these wider CL zones are thickest along the c-axis, and are finely spaced, perpendicular to the b-axis (010).

EMPA trace element maps

Elemental maps of Hf, Y, and Yb reveal distinct zoning patterns that are shared among the zircon grains (Fig. 3). The CL pattern most closely resembles that of Hf concentrations, though the innermost core is best mirrored in the Y concentration map. Changes in U counts follow the overgrowth structures in two zircons (Fig. 3B-C). No changes in Th counts were observed by EMPA analysis for Zr18 (Fig. 3D). The limitation on the minimum spot size of the electron microscopes makes it difficult to delineate these trace element compositions of individual oscillatory zones in CL, particularly for those that are less than a few microns thick. This could also result from the orientation of the grain during analysis such that the incident electron beam was not directly perpendicular to the oscillation bands and results in blurring of the boundaries. Accordingly, the distribution of Y or Yb in zircon grains of Zr9, Zr28, or Zr13 are not as clearly revealed in the EMPA maps (Fig. 3A-C).

We interpret major changes in Hf counts as abrupt compositional changes to distinguish between different zircon crystallization events, particularly between the inherited core and the Jurassic magmatic event (Fig. 3). In all four zircons analyzed, an increase in Hf concentrations occurs at the interface between the two zircon cores and their rims (i.e., within overgrowth structures).

Compositional changes between large, uniform CL growth zones are observed in LCMF14-Zr18 (Fig. 3D) though the small-scale oscillations are not as clearly revealed in the EMPA maps. In Zr18, counts of Hf, Y and Yb are high in the darker-CL regions of the autocrystic domain (Fig. 3D). The intensity of greyscale does not always correlate to regions that have the highest total trace element counts for all elements considered. This is true for Zr18, where the darkest CL region is linked to high Hf counts; changes in Hf clearly distinguish this intermediate region from the innermost inherited core and the autocrystic overgrowth, but shows only low to moderate counts in Y, Yb, and Th.

Fig. 5 Representative time-of-flight mass spectrums for atom probe analysis of zircon. **A** TOF spectra with different peak colors marking the ranges used in the reconstruction. The location of the trace element peak for Al^{2+} is highlighted. **B** Colored peaks correlated to the ions and complexes of the major element constituents of zircon (ZrSiO_4). **C** Minor and trace element peaks identified in the mass spectrum are indicated. The detection of elements at higher Dalton (e.g., mass-to-charge-state ratio > 75) becomes challenging due to increasing complexity relating to peak overlaps and higher background counts

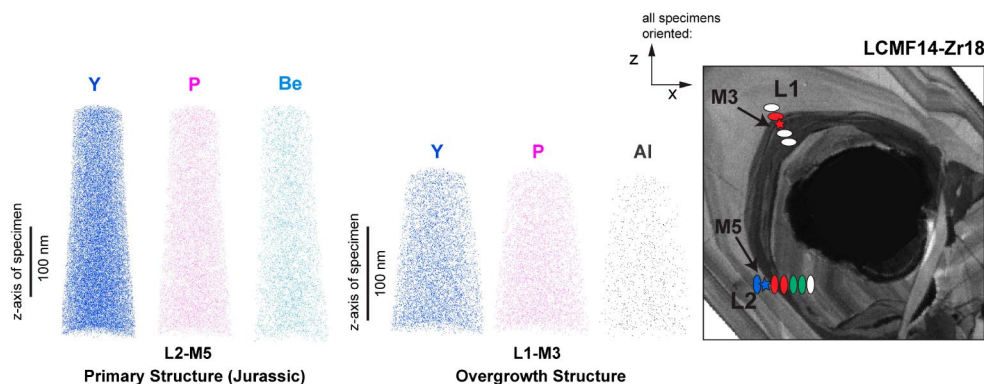
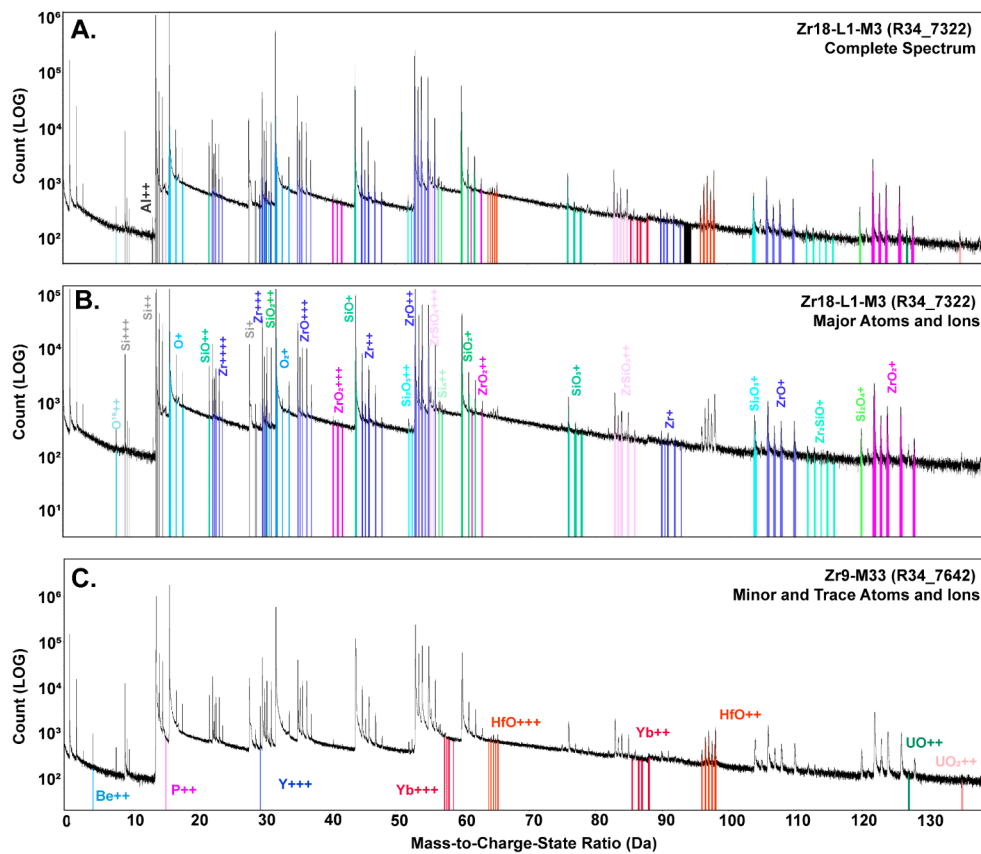


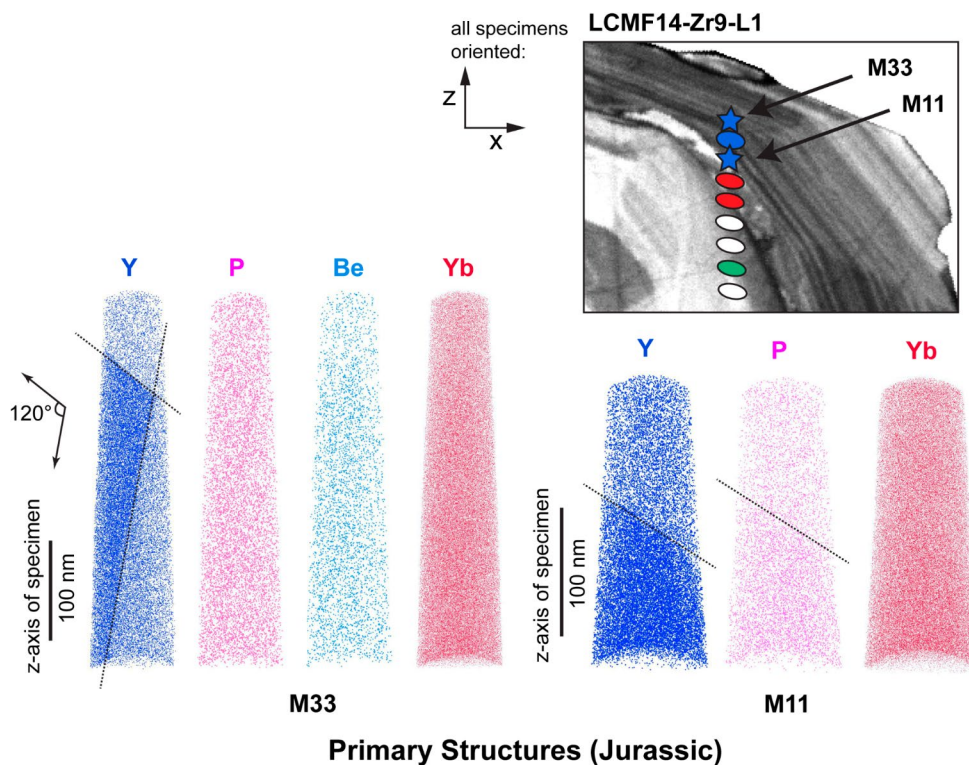
Fig. 6 Trace element reconstructions of two APT specimens from Zr18 within the Jurassic-aged primary structure (L1-M3) and the dark-CL domain overgrowth structure (L2-M5) that separates the inherited core from the autocrystic growth domain; locations indicated by a star from the CL image. Only specimens from the Zr18-L1 transect contain Al.

are located within the Jurassic zircon domain, characterized by small-scale oscillatory zoning. M11 is sampled from the zircon domain closest to the overgrowth structure, thus providing a volume closest to the first autocrystic zircon growth. In M11, the change in Y across the boundary is also observed with changes in P concentrations, where Y concentrations increase from 0.08 to 0.12 at % (i.e., atomic %) and P increases from ~ 0.015 to 0.025 at %. In the M33 specimen, Y concentration more than doubles from 0.08

All specimens from Zr18 exhibit homogenous distributions of Y + P; most elements are also homogeneous but are not shown for simplicity (see SF4). Jurassic zircon domains are characterized by the presence of Y + P + Be

to 0.16 and 0.06 to 0.18 at % across the two boundaries (Fig. 8); to a lesser degree than observed in M11, P increases from 0.04 to 0.05 at % for both. Table 2 provides a comparison of compositional data extracted from each subvolume across the concentration gradient within M11 and M33. In both specimens, there is a slight increase in Yb and Be concentrations across the boundaries (Fig. 8), in comparison to a significant difference in concentrations measured for each zircon sub-volume (Table 2), excluding Hf concentrations.

Fig. 7 Trace element reconstructions of specimens M11 and M33 sampled from oscillatory growth zones in the Jurassic-aged zircon domain. Dashed lines delineate zones of high- and low-concentrations of Y. Changes in both Y + P concentrations are most clearly observed in the M11 reconstruction. In M33, only changes in Y are clearly seen across the boundary; changes in total concentrations are measured within the subvolumes listed in Table 2 for Y + P + Yb and Be in M33



APT specimens from the inherited cores include Zr9-M3 and Zr18-L2-HG-M2 and Zr18-L2-FTM-M2 (Fig. 4; Table 1). Notably, none of the reconstructions sampling xenocrystic cores contain Be or Al, and only the Ordovician core of Zr9 contains P (62 ppma). Additionally, all reconstructions are homogeneous in their trace element distributions (SF4).

Overgrowth structures

Six APT specimens sample zircon domains close to the core-rim interface (i.e., overgrowth structures) between the inherited and autocrystic zircon domains. These include M9 and M10 of Zr9, M3 and M4 of Zr18-L1, and M3 and M4 of Zr18-L2.

Nanoscale planar features and regions of oriented and enriched elemental concentrations were only present in specimen M9 from Zr9 that samples an overgrowth structure (Fig. 9). This specimen has the highest concentrations of Y, Yb, and Be from all zircons analyzed (Table 1). The high Yb concentration of 539 ppma correlates with the Yb enrichment zone observed in the EMPA map (Figs. 3 and 4). Relative to the z-dimension (i.e., depth into sample surface), M9 contains zones of Y-enrichment and a region with Y- and Be-depletions that occur in a different orientation to the Y-enrichments (Fig. 9, SF5). Y-rich regions reach concentrations of 0.14 to 0.17 at %, which persist through the zircon volume at high angles relative to the surface of the

grain. At the base of the sample, a zone of low Y and Be composition crosses at a high angle relative to the z-axis with concentrations of 0.03 and 0.01 at %, respectively. Through the specimen, Yb concentrations increase from 0.4 to 0.6 at % at the base of the specimen. Adjacent to the M9 specimen, M10 of the Zr9-L1 transect, Y and Be were the only trace elements detected, with low concentrations of 39 ppma and 14 ppma, respectively.

Four specimens from Zr18 sample the overgrowth structure characterized by dark-CL intensity between the inherited core and Jurassic domain (Fig. 4). Both specimens from the Zr18-L1 transect are distinct from any other zircon domain analyzed with a detected $^{27}\text{Al}^{++}$ peak at 13.5 Da (Fig. 6). Al concentrations of the L1-M3 and L1-M4 specimens are 8 and 11 ppma, respectively. Specimens L2-M3 and L2-M4 from Zr18 likewise sampled the dark-CL overgrowth structure. Although they do not contain measurable Al concentrations, they resemble L1-M3 and L1-M4 in their Hf, P, U, and Y contents. The average concentrations using all four specimens from this dark-CL domain have Hf ranges from 2031 to 3628 ppma, P ranges from 6 to 49 ppma, U ranges from 100 to 252 ppma, and Y ranges from 64 to 325 ppma.

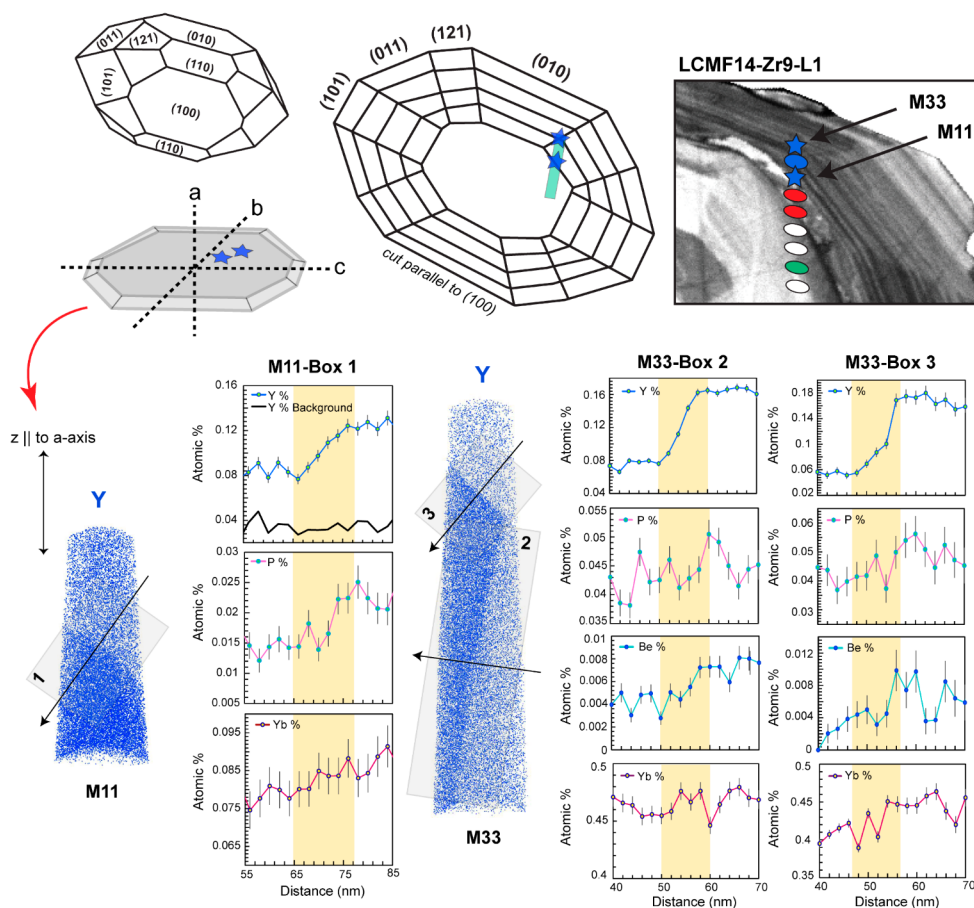


Fig. 8 Concentration profiles for Y, P, and Yb (Be included in M33) across two zircon specimens from the finely spaced oscillatory growth zones in the autocrystic domain of Zr9. The M11 specimen samples the zircon volume closest to the overgrowth structure, providing compositional data of the earliest zircon crystallized from the Jurassic melts. The concentration across the boundary is measured for the volume indicated by the M11 and M33 boxes, with the reconstruction showing the concentration in Y. The lower error associated with the M33 concentrations is due to the larger volume used for determining the

concentration gradient across the boundary. In M11, the change in Y concentration is shown by an increase from 0.08 at % to 0.12 at % (Box 1), whereas Y increases from 0.08 to 0.16 at % along the longest boundary in the M33 specimen (Box 2), and from 0.06 to 0.18 at % along the smaller boundary (Box 3). All three boundaries show a general increase in P relative to the change in Y concentrations (highlighted in yellow); this is also observed for Be in M33. There is a gradual change in Yb across the boundary in M11 and the Box 3 of M33, however, no change is observed in Box 2

Discussion

Tracing sub-micron trace element distributions

Trace element analysis using in-situ techniques (e.g., EMPA, LA-ICP-MS, and SIMS) often measure an average composition from multiple growth bands due to the beam size required (e.g., 10 to 30 μm) relative to the size of many growth features in zircon that are typically sub-micron and down to 10 nm measured here (Fig. 8). In comparison, although APT boasts both high sensitivity and excellent spatial resolution, the overlap of different element peaks (i.e., isobaric interferences with the same mass-to-charge-state ratio) is still an issue for the characterization of mineral compositions, given a mass resolving power ($\text{MRP} = M/\Delta M$) of 1000, together with the challenges that arise for geological

materials that generally have a lower electrical conductivity than metals and therefore the efficiency of field evaporation is reduced (Reddy et al. 2020). Consequently, elemental concentrations measured by APT and LA-ICP-MS may differ substantially (Table 3; see also Saxey et al. 2017). In this study, we rely on EMPA element maps for the μm -scale distribution of trace element distributions within the zircon grain and use APT to compare the relative concentrations of nanoscopic volumes and to visualize the 3-dimensional distribution of trace elements within these volumes.

We use cathodoluminescence imaging of zircon grains to provide the first indication of trace element distribution within the crystal structure (e.g., Hanchar and Miller 1993; Hoskins 2000; Hofmann et al. 2009), in addition to radiation and structural damage (e.g., Hanchar and Rudnick 1995; Nasdala et al. 2006; Anderson et al. 2020). A comparison

Table 2 Comparison of compositional data extracted from the subvolumes of M11 and M33 in Zr9 within the Y-enriched domains and Y-poor domains

atomic %	M11 (whole volume)		M11 (Y-rich volume)		M11 (Y-poor volume)		M33 (whole volume)		M33 (Y-rich volume)		M33 (Y-poor volume)	
	18.48	± 2σ	18.28	± 2σ	18.68	± 2σ	18.38	± 2σ	18.47	± 2σ	18.48	± 2σ
Zr	16.79	0.007	16.85	0.014	16.84	0.014	17.03	0.006	16.93	0.010	16.85	0.011
Si	64.45	0.009	64.51	0.020	64.26	0.020	64.33	0.006	64.25	0.014	64.42	0.014
O		0.010		0.023		0.022		0.008		0.018		0.019
ppma												
Hf	1979	4	2317	8	1892	7	1698	2	1986	6	1779	5
Al	-	-	-	-	-	-	-	-	-	-	-	-
P	70	5	118	10	5	11	24	3	40	6	67	12
Y	420	7	698	19	168	12	542	7	985	18	297	14
Yb	194	1.2	294	27	80	22	224	16	314	38	218	35
U	151	2	244	4	119	3	113	1	90	1	63	2
Be	-	-	-	-	-	-	28	2	43	4	30	7
total ions (Million)	33.8	-	6.9	-	-	-	47	-	12	-	10.6	-

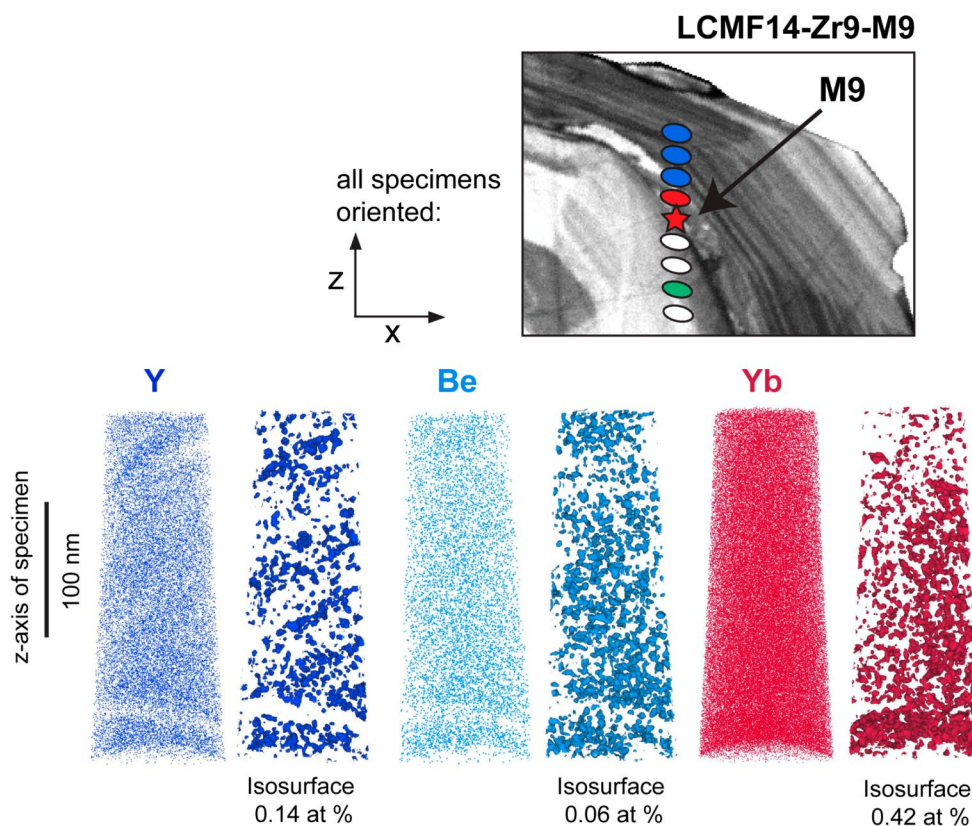
between CL and EMPA trace elemental maps show that CL greyscale intensity does not appear to correspond linearly with regions of higher or lower concentrations (Fig. 3), suggesting that the CL pattern of zircon grains depends intimately on the concentrations of both minor (e.g., Hf) and trace elements. Based on the textural context together with U-Pb ages for different domains (Fig. 2), we attribute abrupt changes in Hf concentration to different crystallization events (i.e. temporally unique). This is particularly evident between the inherited cores and rims that grew during the Jurassic magmatic event (Fig. 3). In comparison, the distribution of Y and Yb as observed in the EMPA maps correlates to specific, fine-scaled features in the CL pattern. Our results are consistent with previous studies that suggest that the dominant CL activators in zircon include the trivalent REEs (e.g., Cesbron et al. 1995; Cherniak et al. 1997b); however, our results indicate a larger contribution from Hf to the CL signal than previously suspected. Additionally, the presence of U⁴⁺ and the radiation damage induced by alpha-decay is thought to suppress CL emission (e.g., Nasdala et al. 2003), while for the grains studied here, the darkest regions of CL intensity in the grains analyzed here are largely attributed to increasing Hf or trace element concentrations within those growth zones.

Igneous zircon trace elements with a crustal affinity

Elevated concentrations of P and Al in zircon have been identified as sensitive indicators for the assimilation of continental crust during the evolution of magmatic compositions (e.g., Burnham and Berry 2017; Zhu et al. 2020; Bell and Kirkpatrick 2021; Ackerson et al. 2021; Bucholz et al. 2022). In particular, the incorporation of Al into zircon is a function of activities for both alumina and H₂O in a melt and the temperature of crystallization (e.g., Trail et al. 2017; Wang and Trail 2019). The activity of alumina is controlled by melt compositional parameters including both proportions of molar ratios of Al₂O₃/(CaO+Na₂O+K₂O) and the aluminum saturation index (K+Na+2Ca)/(Si * Al), whereby excessive Al₂O₃ contents (i.e. peraluminous compositions) are often attributed to contributions from melting of pelitic lithologies (e.g., Chappell and White 1974; Miller 1985). In conjunction with Al, P concentrations in zircon have also been used to discriminate melt sources between metaluminous versus strongly peraluminous compositions, such that higher P concentrations in zircon reflect the enhanced solubility of apatite in peraluminous melts (Bucholz et al. 2022).

Similarly, Be enrichments are associated with granitic systems derived from melting metasedimentary rocks (e.g., Grew 2002); however, the partitioning behavior of Be into zircon has yet to be determined. Metapelites are the most

Fig. 9 Reconstructions for atomic maps and isoconcentration surfaces of Y, Be, and Yb from specimen Zr9-M9 within the overgrowth structure at the innermost interface of the xenocrystic core. Isosurfaces connect regions in the specimen corresponding to the concentration displayed with concentrations of Y at 0.14 atomic %, Be at 0.06 atomic %, and Yb at 0.42 atomic %. The low-angle boundary indicates a region of low concentration for Y + Be (see SF5 for 1D concentration plots). This specimen samples the Yb-rich region observed with the EMPA maps. P was not detected within this volume



Overgrowth Structure

Table 3 Comparison of average bulk concentrations for LCMF14 Autocrystic Zircon

Element	LA-ICP-MS Average (ppm)	APT Average (ppma)
Hf	10,295	1,797
Y	1,113	465
Yb	345	153
U	185	69

LA-ICP-MS average reported in Foley et al. (2023a)

Be-enriched sedimentary rocks, due to the abundance of muscovite with Be contents of 20–120 ppm and additionally cordierite, which contains significant concentrations of Beryllium (London 2015). In this study, APT specimens from the Jurassic zircon domains are clearly distinguishable by the presence of P and Be atoms and are commonly enriched in trace elements (e.g., Y and Yb) relative to the inherited cores. These results agree with those of Foley et al. (2023a, b), as the presence of P, Be, and occasionally Al, are consistent with crystallization of overgrowths from melts derived by partial melting of metasedimentary sources whereby the local breakdown of apatite and muscovite- and/or cordierite-bearing assemblages resulted in the partitioning of these elements into the zircon lattice.

Although P-in-zircon has only recently gained traction as a tracer of parent melt sources (e.g., Burnham and Berry

2017; Ackerson et al. 2021; Bucholz et al. 2022), the partitioning of P is recognized to be important for maintaining charge balance in REE-bearing zircons (Finch et al. 2001; Finch and Hanchar 2003). Owing to crystal-chemical similarities between Y^{3+} and heavy REE^{3+} , the replacement of Zr^{4+} by REE^{3+} in zircon is commonly explained by the coupled xenotime (YPO_4)-type substitution in which P^{5+} replaces Si^{4+} , given by the formula $Y^{3+}/REE^{3+} + P^{5+} = Zr^{4+} + Si^{4+}$. Implicit in this substitution is the assumption that P^{5+} replaces Si^{4+} at the tetrahedral site and REE replace Zr^{4+} at the dodecahedral site (VIII-coordination). Within the specimens measured here, there is a general correlation between increasing concentrations of Y and P observed in the bulk volumes (Table 1); however, this correlation is not always sustained. In the specimens where Y concentrations are low (e.g., Zr18-L2-HG-M2), the absence of P could be due to low concentrations, where the associated P++ peak in the TOF spectra at 15.5 Da is below background levels (i.e., high noise to signal ratio). Conversely, in the Zr9-M9 specimen located within the overgrowth domain, the trace element concentrations are the highest among all zircon volumes analyzed (Table 1), but a P peak was not detected. Therefore, without P the trivalent ions require an alternative charge compensation, either in the form of oxygen defects (e.g., Cherniak et al. 1997b) or by the interstitial

incorporation of +1 ions like H and Li (e.g., Ushikubo et al. 2008; Trail et al. 2016; Wang and Trail 2022); though, Li was not detected in any specimens measured within this study.

The accommodation of Al^{3+} into the zircon structure can be met either by the substitution $\text{Al}^{3+}_{(\text{interstitial})} + 4\text{Y}^{3+} + \text{P}^{5+} = 4\text{Zr}^{4+} + \text{Si}^{4+}$ (e.g., Hoskin et al. 2000) or by $\text{Al}^{3+} + \text{H}^+ = \text{Si}^{4+}$ (e.g., Trail et al. 2011). In the two APT specimens containing Al (Zr18-L1-M3 and M4; Table 1), the first equation offers a suitable charge balancing substitution, as both Y and P are present. Though, charge balance with H cannot be evaluated using APT, due to the residual presence of H in the chamber and on the specimen shank. A similar substitution can be applied for Be, where $\text{Be}^{2+}_{(\text{interstitial})} + 3\text{Y}^{3+} + \text{P}^{5+} = 3\text{Zr}^{4+} + \text{Si}^{4+}$ (e.g., Reddy et al. 2016). This substitution can apply to the autocrystic domains, where Be is present together with P and Y (Table 1). However, within the overgrowth structure of Zr9 (M9 and M10), concentrations of Be and Y cannot be balanced with this substitution, due to the absence of P. In IV-coordination, Si^{4+} and Be^{2+} have a similar ionic radius of 0.26 Å and 0.27 Å respectively (Shannon 1976), though a 1:1 substitution will result in a charge deficiency. If Be^{2+} is interstitial or substituted in the Si^{4+} site, a 2+ charge would thus be required to maintain charge balance (e.g., 2 H^+); alternatively, charge balance could be maintained with Be^{2+} on both the Si^{4+} site and an interstitial site.

Zircon nanostructures

We targeted zircon grains with complex interface domains between an inherited core and younger autocrystic domain to characterize the nanoscale structure and chemistry and provide information pertaining to the melt both prior to and after dissolution. During crystallization, impurities to the zircon ZrSiO_4 structure result from the partitioning of minor (Hf) and trace element substitution. Consequently, the heterogeneous manifestations of these trace elements at the atomic scale (e.g., point defects, Peterman et al. 2019; low-angle boundaries, Reddy et al. 2016; clustering due to alpha-decay, Valley et al. 2015; Peterman et al. 2016) can provide information about the nanoscopic growth environment and/or post growth modification to the crystal lattice (e.g., diffusion, annealing, etc.).

For the three transects sampled here, only one analyzed volume within an overgrowth structure revealed complex redistribution of trace elements in sample Zr9 (Fig. 9). Relative to the analyzed surface, these nanostructures manifest in the interface domain of zircon sample Zr9-M9 as (a) Y-enriched regions that occur at high angles, relative to the z-axis, and (b) a low-angle zone characterized by the depletion of Y and Be (Fig. 9). It is possible that the accumulation

of trace elements along such features in Zr9-M9 occurred via mineral replacement reactions (e.g., Putnis 2000; Geisler et al. 2007) either by (1) solid-state diffusion driven reactions within a fluid-dominated regime (e.g., recrystallization during metamorphism; Hoskin and Black 2000) or (2) during chemical re-equilibration by coupled dissolution-precipitation processes within a fluid or melt phase (e.g., Peterman et al. 2019). During re-equilibration, zircon will react with a solution (aqueous fluid or melt) to produce a rim with a lower concentration of the solid solution phase (e.g., xenotime, YPO_4) and produce a reaction domain that is enriched in the components of the solid solution phase (e.g., HfSiO_4 , USiO_4 , ThSiO_4 , or YPO_4 ; Geisler et al. 2007). For either mechanism, inclusions of these solid-solution phases will be present if the eutectic is reached, and an increase in porosity within the crystalline structure will occur. Peterman et al. (2019) observed similar microstructural features by APT within a complex interface domain that separated a magmatic zircon core from a younger metamorphic rim where they explained trace element accumulation of Y, P, and Yb or U along the planar features by solid-state reaction within a transgressive, fluid-mediated reaction front (i.e., mechanism 1 above). Similar to Peterman et al. (2019), we observe a zircon volume (Zr9-M9) that is extremely enriched in trace element concentrations of Y, Be, and Yb that is immediately followed by a volume depleted in trace elements (Zr9-M10; Table 1). However, neither the enriched (M9) nor depleted volume (M10) within this interface region contains P and, therefore, cannot be simply explained by the xenotime solution substitution.

Alternatively, enrichment of trace elements at the inherited cores interface could derive from the dissolution of the inherited core (i.e., resorption of the grain) leading to the local enrichment of the slow diffusing elements within a melt (mechanism 2 above). Though, the APT volume that samples the portion of the inherited core contains elevated concentrations of P with no detectable Yb (Zr9-M3; Table 1), whereas Zr9-M9 contains no detected P and is extremely enriched in Yb. Furthermore, the Zr9-M9 specimen also contains elevated Be concentrations (170 ppma), where the presence of Be has only been linked to the Jurassic anatexis event (Table 1). Therefore, the enrichment of trace elements in M9 could not have been sourced solely from the local dissolution or re-equilibration of the inherited grain.

Based on the presence of Be, we interpret the interface domain to reflect growth during the Jurassic anatexis event, following the breakdown of Be-rich minerals (e.g., muscovite, cordierite). We suggest that the linear features of Y-enrichments formed during primary crystallization, and not as a result of re-equilibration via one of the mineral replacement reactions mentioned above, or due to deformation-induced trace element mobility. Instead, the interface

region of Zr9 was likely precipitated during alternating periods of local zircon undersaturation followed by saturation. Dissolution and subsequent re-crystallization reactions in the presence of a melt phase also explain the presence of the low-angle grain boundary that reflects misorientation of the crystal lattice. During growth, crystallization proceeded with zircon that was not epitaxial to the inherited core. Once the melt reached zircon-saturated conditions, growth characterized by small-scaled oscillatory zones is separated from the interface domain by a conformable boundary.

Oscillatory Zonation in Zircon

Although oscillatory growth zones are observed across a variety of igneous minerals, the origin and significance are still debated (e.g., Melnik and Bindeman 2018 and references within). Zircon growth requires diffusion of elements (Zr-Si-O) through a melt towards an advancing stoichiometric crystallographic face. Changes relating to crystal growth at bulk saturation – either being an impediment of growth (local undersaturation and/or step pinning by impurities) or rapid crystallization (supersaturation) – result in localized differences in growth patterns that are reflected in the observed CL pattern. Oscillation growth zones are understood to reflect the heterogeneous distribution of trace elements within crystals (Hanchar and Miller 1993) and are commonly observed in igneous zircon (Hoskin and Schaltegger 2003). Large, uniform oscillatory growth zones in zircon crystals are thought to represent episodes of growth in a saturated environment, where major changes in trace element composition reflect external forcing due to changing magmatic conditions and compositions (e.g., magma mixing or replenishing events; Claiborne et al. 2010; Gagnevin et al. 2010). In comparison, fine-scale oscillatory zoning is likely controlled on the nanoscale by processes occurring at the zircon-melt interface (Vavra 1990; Hoskins 2000; Fowler et al. 2002; Hoskins and Schaltegger 2003; Melnik and Bindeman 2018).

While both zircon grains analyzed by APT are characterized by magmatic oscillations, the band spacing in Zr9 is considerably smaller (e.g., $\sim 1 \mu\text{m}$ spacing) than for Zr18 where the APT samples were selected. Based on the positioning of the APT specimens relative to the crystallographic growth zones in Zr9, we interpret the two volumes of Zr9-M11 and M33 as both intersecting across oscillatory zones (Fig. 8). In both volumes, two distinct regions of higher and lower concentrations are observed primarily by changes in Y concentration and to a lesser extent changes in P (Fig. 7) across a boundary of 12 and 10 nm, respectively (Fig. 8). Bulk concentrations calculated for each sub volume across the plane indicates that most of the detected trace element contents (Y, P, Yb, and Be) are similarly divided between

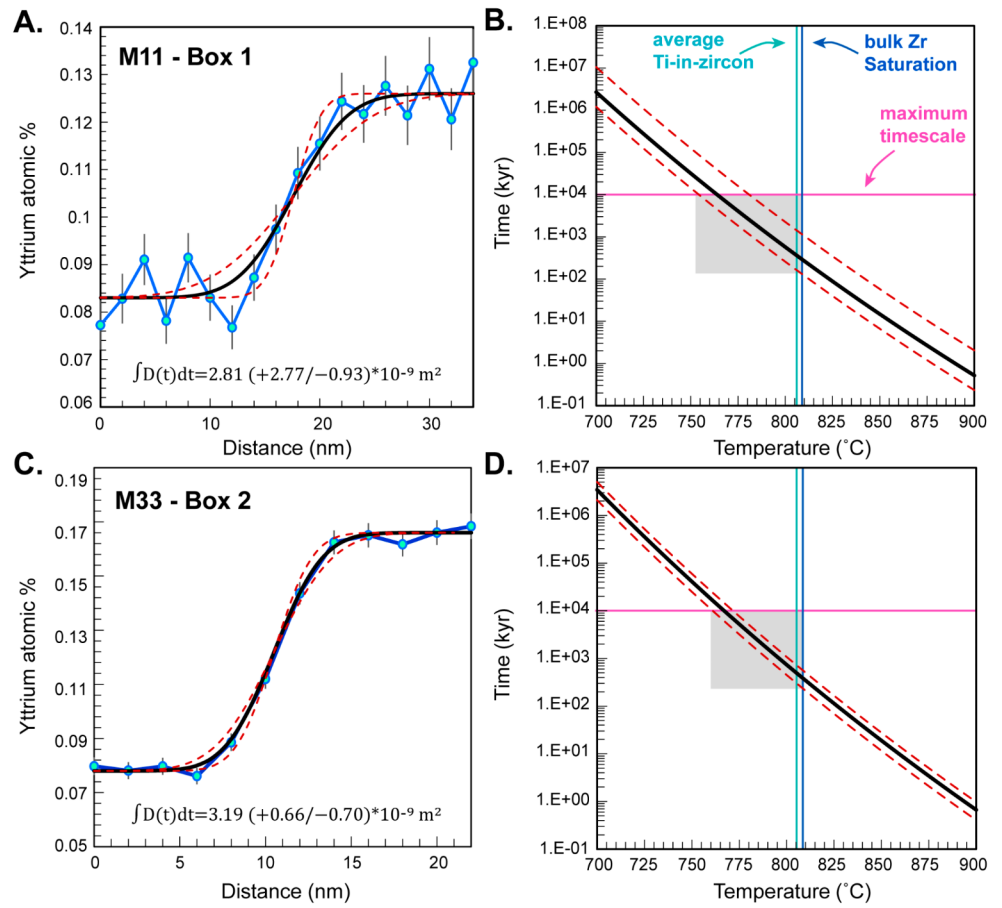
lower and higher concentrations (Table 2), while Hf remains consistent across the volumes. In M11 and M33, P generally follows the change in Y concentration across the boundary, although the ‘step’ is not as clearly observed, while Yb (and Be in M33) is observed to have a slight increase across the boundaries. This coupled behavior between Y and P in M11 is more consistent with the xenotime substitution mechanism; however, the lack of a clear coupled substitution in M33 suggests that multiple substitution mechanisms may operate. It is likely that other REE³⁺ elements follow a similar trend as Y across the concentration boundary given the similarity in size and geochemical behavior. However, the REE cannot be distinguished in the zircon APT TOF spectra due to peak overlaps and because they are distributed across multiple peaks throughout the spectra, including both elemental and oxide charge states, and therefore are often below background detection levels.

These two reconstructions provide APT sampling of a boundary between oscillatory growth zones in igneous zircon. Proposed mechanisms for generating fine-scaled oscillations include: (1) equilibrium trace element partitioning that is limited by diffusion in the melt (e.g., diffusive boundary layers; Smith et al. 1955; Albarède and Bottinga 1972; Lasaga 1982), (2) non-equilibrium growth relating to surface-enrichment impurities/poisoning (e.g., Watson 1996a), and (3) crystallographic controlled growth zoning (e.g., sector zoning; Watson and Liang 1995). Based on available diffusivities of trace elements in silicate melts (e.g., Holycross and Watson 2018), growth velocity boundary layer models typically predict boundaries between compositional zones that are more broad (e.g. Watson 1996b; Watson and Müller 2009) than what is observed in the samples studied here ($\sim 10 \text{ nm}$ width, as shown in Fig. 10). This would seem to indicate that either an as-yet unidentified mechanism has led to these extremely sharp boundaries between oscillatory zones, or that at least one of the mechanisms mentioned above is capable of generating far sharper boundaries than previously thought.

Y diffusion modeling and growth zoning implications

Although the growth mechanism for generating the oscillations with extremely sharp boundaries described above remains unclear, the portion of the zircon from where these two APT volumes are sampled are considered to reflect crystallization from a Zr saturated melt; therefore, diffusion profiles across these two boundaries provide a timescale between zircon saturation to eruption. To constrain the residence time of zircon in upper crustal reservoirs, we have modeled the Y concentration profiles observed in samples Zr9-M11 and -M33 (Fig. 8). Our diffusion calculations

Fig. 10 Diffusion profiles fit across the two Y concentration gradients in M11 (Box 1, Fig. 8) and M33 (Box 2, Fig. 8). Panels A and C show the measured profiles (blue line) and modeled fits (black lines) with uncertainties (red dashed lines). Panels B and D show the timescale as a function of temperature retrieved from the profiles shown in A and C, respectively. Both the average temperature calculated using Ti-in-zircon and bulk zircon saturation thermometry for ignimbrite sample LCMF14 is calculated at ~810 °C (Foley et al. 2023a). A maximum timescale of 10 Myr is determined considering the spatial migration of magmatism in the CASP; shaded regions represent the timescales calculated considering temperatures between zircon-based thermometers and the maximum timescale considered. See text for further details



assume a step function as the initial profile, plane-sheet geometry, and a constant diffusion coefficient (i.e., isothermal diffusion), which corresponds to the solution to the diffusion equation described by:

$$\frac{C(x, t) - C_{min}}{C_{max} - C_{min}} = \frac{1}{2} \operatorname{erfc} \left(\frac{x - x_0}{2\sqrt{Dt}} \right) \quad (1)$$

Where $C(x, t)$ is the concentration of Y at distance x and time t , C_{min} and C_{max} are the initial concentrations on either side of the step function, x_0 is the initial position of the interface between C_{min} and C_{max} and D is the diffusion coefficient. Because there are no published diffusion coefficients for Y in zircon, we have used the D_y in zircon data from Cherniak et al. (1997b). D_y in zircon should be a reasonable proxy for Y, due to the identical charge, similar ionic radii, and general similarity in geochemical behavior between Y and REEs (Hanchar et al. 2001; Finch et al. 2001).

The Y profiles extracted from samples M11 and M33, along with the fits to the data using Eq. 1, are shown in Fig. 10. Samples M11 and M33 yield $\int D(t) dt$ values of $2.81 (+2.77/-0.93) * 10^{-9} \text{ m}^2$ and $3.19 (+0.66/-0.70) * 10^{-9} \text{ m}^2$, respectively. These two values agree within error, although there is less error associated with M33, due to the

reduced scatter in Y data with higher counting statistics. Because we do not have a tight constraint for the temperature-time path over which diffusion occurred, we have used these $\int D(t) dt$ values to calculate the timescale that would correspond to isothermal diffusion between 700 and 900 °C (Fig. 10). It is important to note that the calculations summarized in Fig. 10 represent maximum timescales for each given temperature. This is due to the fact that we have assumed a step function as the initial profile, despite the possibility that there could have been initial growth zonation of Y. This is especially true because the measured Y profiles are extremely short; therefore, the actual residence time of these zircons, corresponding to any given temperature, could have been significantly shorter than what is indicated in Fig. 10.

Although we do not have tight constraints on the pressure-temperature-time path over which the EQC magmas were generated, we place a maximum timescale constraint of 10 Myr based on the spatial migration of magmatism in the CASP, relating to the differential rollback of the subducting slab beneath Patagonia (cf. Foley et al. 2024). Estimates for temperatures are determined using the average of calculated Ti-in-zircon temperatures, together with the bulk Zirconium saturation temperature, both of which are ~810 °C (Foley et

al. 2023a). We note the limitation of these two thermometers for the LCMF14 ignimbrite sample, as both the TiO_2 activity and melt composition were estimated for this sample due to extensive secondary alteration of the bulk-rock sample (e.g., Foley et al. 2023b). Based on these constraints, timescales of diffusion are on the order of $\sim 10,000$ years to 10 Myr over temperatures of 810 to 750 °C, respectively. Future work to constrain the thermal evolution of the EQC dacite ignimbrites will aid to provide an estimate for the timescales of zircon growth; though this temperature range is generally consistent with those of natural dacite compositions (e.g., Blundy and Cashman 2001).

Conclusions

This research combines methods of cathodoluminescence imaging (CL), electron microprobe elemental maps (EMPA), and Atom Probe Tomography (APT) that presents data pertaining to the distribution and abundances of minor and trace elements in igneous zircon. This data provides novel insights into processes relating to crystal growth and information pertaining to the local melt compositions(s) during crustal anatexis. For the zircon grains studied here, the incorporation of older continental crust is evident by the inherited zircons in the Los Córdobes ignimbrite from the El Quemado Complex. The presence of P and Be in the autocrystic zircon domains further supports a model of crystallization from melts derived by partial melting of metasedimentary sources wherein the local enrichment of these trace elements in the melt is sourced from the breakdown of muscovite and cordierite-bearing assemblages. During anatexis, complex reaction textures at the interface (i.e., overgrowth structures) of the inherited zircon core demonstrate dynamic dissolution/precipitation reactions that occurred prior to bulk zircon saturation in the magma. In comparison, the homogeneous distribution of minor and trace element species indicates that the inherited zircon grains from Zr9 and Zr18 remained undisturbed during anatexis.

Significantly, these APT volumes provide nanoscale sampling of boundaries between oscillatory growth zones in an igneous zircon. Reconstructions reveal compositional zoning of Y and, to a lesser extent P, which appear as high-angle, planar features with respect to the atom probe specimen, that coincide with the fine-scaled oscillatory zones in the Jurassic-aged autocrystic growth domains. These extremely short Y concentration boundaries measured on the order of 10 to 12 nm are difficult to reconcile with proposed mechanisms for generating fine-scaled oscillations. This suggests that either an as-yet unidentified mechanism has led to these extremely sharp boundaries between oscillatory zones, or that at least one of the mechanisms presented

can generate far sharper boundaries than previously considered. Diffusion calculations fit to the concentration profiles in Y provide estimates for the timescales over which zircon grew prior to eruption; we constrain a temperature window over 810 to 750 °C that corresponds to timescales on the order of 10,000 years to 10 Myr, respectively. We acknowledge the limitation placed by the lack of published diffusion coefficients for Y, which could necessitate a reassessment of these timescales calculated. Regardless, we emphasize the potential for APT as a technique to measure diffusional profiles that, at the time of writing, are unobtainable by other methods.

Supplementary Information The online version contains supplementary material available at <https://doi.org/10.1007/s00410-024-02166-5>.

Acknowledgements We thank Martin Robyr (ISTE, UNIL) for his assistance with the Electron Microprobe Analyses and Christian Zaubitzer (ScopeM, ETH) for access and support on the Focused Ion Beam – Scanning Electron Microscope. We also thank Jim Watkins for comments and suggestions on this manuscript. We appreciate the comments and suggestions made by editor Dante Canil and both reviewers Elizabeth Bell and Steven Reddy that helped improve the quality of this manuscript. This research was funded by the Swiss National Science Foundation (SNSF) Ambizione grant PZ00P2_173988 to EMB. MLF was supported by SNSF grant 200021_175808 to BP throughout the course of this research.

Author contributions MLF and EMB contributed to the study concept and design. Material preparation, data collection, and reduction were conducted by MLF and SSAG. Diffusion models were produced by MLF and EMB. BP and LPB supervised throughout the duration of this study. The first draft was written by MLF and all authors comment on previous versions of the manuscript. All authors read and approved the final manuscript.

Funding Open access funding provided by University of Lausanne

Data availability All data obtained during this study are included in this published article and its supplementary files.

Declarations

Conflict of interest We declare that we have no conflict of interest.

Open Access This article is licensed under a Creative Commons Attribution 4.0 International License, which permits use, sharing, adaptation, distribution and reproduction in any medium or format, as long as you give appropriate credit to the original author(s) and the source, provide a link to the Creative Commons licence, and indicate if changes were made. The images or other third party material in this article are included in the article's Creative Commons licence, unless indicated otherwise in a credit line to the material. If material is not included in the article's Creative Commons licence and your intended use is not permitted by statutory regulation or exceeds the permitted use, you will need to obtain permission directly from the copyright holder. To view a copy of this licence, visit <http://creativecommons.org/licenses/by/4.0/>.

References

- Ackerson MR, Trail D, Buettner J (2021) Emergence of peraluminous crustal magmas and implications for the early earth. *Geochem Persp Lett* 17:50–54. <https://doi.org/10.7185/geochemlet.211450>
- Albarède F, Bottinga Y (1972) Kinetic disequilibrium in trace element partitioning between phenocrysts and host lava. *Geochemica et Cosmochim Acta* 36:141–156. [https://doi.org/10.1016/0016-7037\(72\)90003-8](https://doi.org/10.1016/0016-7037(72)90003-8)
- Anderson AJ, Hanchar JM, Hodges KV, van Soest MC (2020) Mapping radiation damage zoning in zircon using Raman spectroscopy: implications for zircon chronology. *Chem Geol* 538:119494. <https://doi.org/10.1016/j.chemgeo.2020.119494>
- Bea F, Montero P, González-Lodeiro F, Talaveria C (2007) Zircon inheritance reveals exceptionally fast crustal magma generation processes in Central Iberia during the Cambro-Ordovician. *J Petrol* 48:2327–2339. <https://doi.org/10.1093/petrology/egm061>
- Bell EA, Kirkpatrick HM (2021) Effects of crustal assimilation and magma mixing on zircon trace element relationships across the Peninsular Ranges Batholith. *Chem Geol* 586:120616. <https://doi.org/10.1016/j.chemgeo.2021.120616>
- Bloch EM, Jollands MC, Tollan P, Plane F, Bouvier A-S, Hervig R, Berry AJ, Zaubitzer C, Escrig S, Müntener O, Ibáñez-Mejía M, Alleon J, Meibom A, Baumgartner LP, Marin-Carbonne J, Newville M (2022) Diffusion anisotropy of Ti in zircon and implications for Ti-in-zircon thermometry. *Earth Planet Sci Lett* 588. <https://doi.org/10.1016/j.epsl.2021.117317>
- Blum TB, Darling JR, Kelly TF, Larson DJ, Moser DE, Perez-Huerta A, Prosa TJ, Reddy SM, Reinhard DA, Ulfig RM, Valley JW (2018) Best Practices for Reporting Atom Probe Analysis of Geological Materials. In *Microstructural Geochronology* (eds D.E. Moser, F. Corfu, J.R. Darling, S.M. Reddy and K. Tait). <https://doi.org/10.1002/9781119227250.ch18>
- Blundy JB, Cashman K (2001) Ascent-driven crystallization of dacite magmas at Mount St Helens, 1980–1986. *Contrib Mineral Petrol* 140:631–650. <https://doi.org/10.1007/s004100000219>
- Bucholz CE, Liebmann J, Spencer CJ (2022) Secular variability in zircon phosphorous concentrations prevents simple petrogenetic classification. *Geochemical Perspective Lett* 24:12–16. <https://doi.org/10.7185/geochemlet.2240>
- Burnham AD, Berry AJ (2017) Formation of Hadean granites by melting of igneous crust. *Nat Geosci* 10:457–461. <https://doi.org/10.1038/ngeo2942>
- Cesbron F, Blanc P, Ohnenstetter D, Rémond G (1995) Cathodoluminescence of Rare Earth Doped zircons. I. Their possible use as reference materials. *Scanning Microscopy Supplement* 9:35–56
- Chappell BW, White AJ (1974) Two contrasting granite types. *Pac Geol* 8:173–174
- Cherniak DJ, Watson EB (2003) Diffusion in Zircon. *Rev Mineral Geochem* 53:113–143. <https://doi.org/10.2113/0530113>
- Cherniak DJ, Hanchar JM, Watson EB (1997a) Diffusion of tetravalent cations in zircon. *Contrib Mineral Petrol* 127:383–390. <https://doi.org/10.1007/s004100050287>
- Cherniak DJ, Hanchar JM, Watson EB (1997b) Rare-earth diffusion in zircon. *Chem Geol* 134:289–301. [https://doi.org/10.1016/S0009-2541\(96\)00098-8](https://doi.org/10.1016/S0009-2541(96)00098-8)
- Claiborne LL, Miller CF, Wooden JL (2010) Trace element composition of igneous zircon: a thermal and compositional record of the accumulation and evolution of a large silicic batholith, Spirit Mountain, Nevada. *Contrib Mineral Petrol* 160:511–531. <https://doi.org/10.1007/s00410-010-0491-5>
- Finch RJ, Hanchar JM (2003) Structure and Chemistry of Zircon and Zircon-Group Minerals. *Rev Mineral Geochem* 53:1–25. <https://doi.org/10.2113/0530001>
- Finch RJ, Hanchar JM, Hoskin PWO, Burns PC (2001) Rare-earth elements in synthetic zircon: part 2. A single-crystal X-ray study of xenotime substitution. *Am Mineral* 86:681–689. <https://doi.org/10.2138/am-2001-5-608>
- Foley ML, Putlitz B, Baumgartner LP, Renda EM, Ulianov A, Siron G, Chiaradia M (2023a) Identifying crustal contributions in the Patagonian Chon Aike Silicic large Igneous Province. *Contrib Miner Petrol* 178:80. <https://doi.org/10.1007/s00410-023-02065-1>
- Foley ML, Putlitz B, Baumgartner LP, Bégué F, Siron G, Kosmal A (2023b) Generating large volumes of crust-derived high $\delta^{18}\text{O}$ rhyolites in the Chon Aike Silicic large Igneous Province. *Patagonia Geosph* 19:4. <https://doi.org/10.1130/GES02551.1>
- Foley ML, Gaynor SP, Putlitz B, Baumgartner LP (2024) High-precision U-Pb geochronology of an ignimbrite flare-up in a silicic large igneous province (Chon Aike, Patagonia). *Lithos* 482–483:107693. <https://doi.org/10.1016/j.lithos.2024.107693>
- Fougerouse D, Geisler T, Reddy SM, Aleshin M, Martin L, Doucet LS, Quadir Z, Saxey D, Rickard W (2024) Melt-mediated re-equilibration of zircon produced during meltdown of the Chernobyl reactor. *Am Mineral* 109:8–14. <https://doi.org/10.2138/am-2022-8824>
- Fowler A, Prokoph A, Stern R, Dupuis C (2002) Organization of oscillatory zoning in zircon: analysis, scaling, geochemistry, and model of a zircon from Kipawa, Quebec. *Can Geochim et Cosmochemica Acta* 66:311–328. [https://doi.org/10.1016/S0016-7037\(01\)00774-8](https://doi.org/10.1016/S0016-7037(01)00774-8)
- Gagnevin D, Daly JS, Kronz A (2010) Zircon texture and chemical composition as a guide to magmatic processes and mixing in a granitic environment and coeval volcanic system. *Contrib Mineral Petrol* 159:579–596. <https://doi.org/10.1007/s00410-009-0443-0>
- Geisler T, Schaltegger U, Tomaschek F (2007) Re-equilibration of Zircon in Aqueous fluids and melts. *Elements* 3:43–50. <https://doi.org/10.2113/gselements.3.1.43>
- Grew ES (2002) Beryllium in Metamorphic environments (emphasis on aluminous compositions). *Rev Mineral Geochem* 50:487–549. <https://doi.org/10.2138/rmg.2002.50.12>
- Gust DA, Biddle KT, Phelps DW, Uliana MA (1985) Associated Middle to late jurassic volcanism and extension in Southern South America. *Tectonophysics* 116:223–253. [https://doi.org/10.1016/0040-1951\(85\)90210-0](https://doi.org/10.1016/0040-1951(85)90210-0)
- Hanchar JM, Miller CF (1993) Zircon zonation patterns as revealed by cathodoluminescence and backscattered electron images: implications for interpretation of complex crustal histories. *Chem Geol* 110:1–13. [https://doi.org/10.1016/0009-2541\(93\)90244-D](https://doi.org/10.1016/0009-2541(93)90244-D)
- Hanchar JM, Rudnick RL (1995) Revealing hidden structures: the application of cathodoluminescence and back-scattered electron imaging to dating zircon from lower crustal xenoliths. *Lithos* 36:289–303. [https://doi.org/10.1016/0024-4937\(95\)00022-4](https://doi.org/10.1016/0024-4937(95)00022-4)
- Hanchar JM, Finch RJ, Hoskin PWO, Watson EB, Cherniak DJ, Mariano AN (2001) Rare earth elements in synthetic zircon: part 1. Synthesis, and rare earth element and phosphorous doping. *Am Mineral* 86:667–680. <https://doi.org/10.2138/am-2001-5-607>
- Harrison TM, Watson EB (1983) Kinetics of zircon dissolution and zirconium diffusion in granitic melts of variable water content. *Contrib Miner Petrol* 84:66–72. <https://doi.org/10.1007/BF01132331>
- Hofmann AE, Valley JW, Watson EB, Cavosie AJ, Eiler JM (2009) Sub-micron scale distributions of trace elements in zircon. *Contrib Mineral Petrol* 158:317–335. <https://doi.org/10.1007/s00410-009-0385-6>
- Holycross ME, Watson EB (2018) Trace element diffusion and kinetic fractionation in wet rhyolitic melt. *Geochim Cosmochim Acta* 232:14–29. <https://doi.org/10.1016/j.gca.2018.04.006>
- Hoskins PWO (2000) Patterns of chaos: fractal statistics and the oscillatory chemistry of zircon. *Geochim Cosmochim Acta* 64:1905–1923. [https://doi.org/10.1016/S0016-7037\(00\)00330-6](https://doi.org/10.1016/S0016-7037(00)00330-6)

- Hoskins PWO, Black LP (2000) Metamorphic zircon formation by solid-state recrystallization of protolith igneous zircon. *J Metamorph Geol* 18:423–439. <https://doi.org/10.1046/j.1525-1314.2000.00266.x>
- Hoskins PWO, Schaltegger U (2003) The composition of Zircon and Igneous and Metamorphic Petrogenesis. *Rev Mineral Geochem* 53:27–62. <https://doi.org/10.2113/0530027>
- Hoskins PWO, Kinny PD, Wyborn D, Chappell BW (2000) Identifying Accessory Mineral saturation during differentiation in Granitoid Magmas: an Integrated Approach. *J Petrol* 41:1365–1396. <https://doi.org/10.1093/petrology/41.9.1365>
- Kinny PD, Maas R (2003) Lu-Hf and Sm-Nd isotope systems in zircon. *Rev Mineral Geochem* 53:327–341. <https://doi.org/10.2113/0530327>
- Kunz BE, Regis D, Engi M (2018) Zircon ages in granulite facies rocks: decoupling from geochemistry above 850°C? *Contrib Miner Petrol* 173:26. <https://doi.org/10.1007/s00410-018-1454-5>
- La Fontaine A, Piazzolo S, Trimby P, Yang L, Cairney JM (2017) Laser-assisted Atom Probe Tomography of Deformed minerals: a Zircon Case Study. *Microsc Microanal* 23:404–413. <https://doi.org/10.1017/S1431927616012745>
- Lasaga AC (1982) Towards a master equation in crystal growth. *Am J Sci* 282:1264–1288
- London D (2015) Reading pegmatites: part 1 – what Beryl says. *Rocks Minerals* 90:138–153
- Melnik OE, Bindeman IN (2018) Modeling of trace element zoning patterns in accessory minerals with emphasis on the origin of micrometer-scale oscillatory zoning in zircon. *Am Mineral* 103:355–368. <https://doi.org/10.2138/am-2018-6182>
- Miller CF (1985) Are strongly peraluminous magmas derived from pelitic sedimentary sequences? *J Geol* 14:804–805
- Miller JS, Matzel JEP, Miller CF, Burgess SD, Miller RB (2007) Zircon growth and recycling during the assembly of large, composite arc plutons. *J Volcanol Geoth Res* 167:282–299. <https://doi.org/10.1016/j.jvolgeores.2007.04.019>
- Möller A, O'Brien PJ, Kennedy A, Kröner A (2003) Linking growth episodes of zircon and metamorphic textures to zircon chemistry: an example from the Ultra high-temperature granulites of Rogaland (SW Norway). *Geol Soc Lond Special Publications* 220:65–81. <https://doi.org/10.1144/GSL.SP.2003.220.01.04>
- Nasdala L, Zhang M, Kempe U, Panczer G, Gaft M, Andrut M, Plötze M (2003) Spectroscopic methods applied to zircon. In: Hanchar JM, Hoskin PWO (eds) *Zircon. Reviews in mineralogy and geochemistry*. Mineralogical Society of America 427–467. <https://doi.org/10.2113/0530427>
- Nasdala L, Kronz A, Hanchar JM, Tichomirowa M, Davis DW, Hofmeister W (2006) Effects of natural radiation damage on back-scattered electron images of single crystals of minerals. *Am Mineral* 91:1739–1746. <https://doi.org/10.2138/am.2006.2241>
- O'Brien TM, Miller EL (2014) Continuous zircon growth during long-lived granulite facies metamorphism: a microtextural, U-Pb, Lu-Hf and trace element study of Caledonian rocks from the Arctic. *Contrib Miner Petrol* 168:1071. <https://doi.org/10.1007/s00410-014-1071-x>
- Pankhurst RJ, Rapela CR (1995) Production of jurassic rhyolite by anatexis of the lower crust of Patagonia. *Earth Planet Sci Lett* 134:23–36. [https://doi.org/10.1016/0012-821X\(95\)00103-J](https://doi.org/10.1016/0012-821X(95)00103-J)
- Pankhurst RJ, Leat PT, Sruga P, Rapela CW, Márquez M, Storey BC, Riley TR (1998) The Chon Aike silicic igneous province of Patagonia and related rocks in Antarctica: a silicic large igneous province. *J Volcanol Geoth Res* 81:113–136. [https://doi.org/10.1016/S0377-0273\(97\)00070-X](https://doi.org/10.1016/S0377-0273(97)00070-X)
- Pankhurst RJ, Riley TR, Fanning CM, Kelley SP (2000) Episodic silicic volcanism in Patagonia and the Antarctic Peninsula: chronology of magmatism associated with the break-up of Gondwana. *J Petrol* 41:603–625. <https://doi.org/10.1093/petrology/41.5.605>
- Peterman EM, Reddy SM, Saxey DW, Snoeyenbos DR, Rickard WDA, Fougereuse D, Kylander-Clark ARC (2016) Nanogeochronology of discordant zircon measured by atom probe microscopy of Pb-enriched dislocation loops. *Sci Adv* 2. <https://doi.org/10.1126/sciadv.1601318>
- Peterman EM, Reddy SM, Saxey DW, Fougereuse D, Snoeyenbos DR, Rickard WDA (2019) Nanoscale processes of trace element mobility in metamorphosed zircon. *Contrib Miner Petrol* 174. <https://doi.org/10.1007/s00410-019-1631-1>
- Piazzolo S, La Fontaine A, Trimby P, Harley S, Yang L, Armstrong R, Cairney JM (2016) Deformation-induced trace element redistribution in zircon revealed using atom probe tomography. *Nat Commun* 7:1–7. <https://doi.org/10.1038/ncomms10490>
- Putnis A (2000) Mineral replacement reactions: from macroscopic observations to microscopic mechanisms. *Mineral Mag* 66:689–708. <https://doi.org/10.1180/0026461026650056>
- Reddy SM, Van Riessen A, Saxey DW, Johnson TE, Rickard WDA, Fougereuse D, Fischer S, Prosa TJ, Rice KP, Reinhard DA, Chen Y, Olson D (2016) Mechanisms of deformation-induced trace element migration in zircon resolved by atom probe and correlative microscopy. *Geochim Cosmochim Acta* 195:158–170. <https://doi.org/10.1016/j.gca.2016.09.019>
- Reddy SM, Saxey DW, Rickard WD, Fougereuse D, Montalvo SD, Verberne R, Van Riessen A (2020) Atom probe tomography: development and application to the Geosciences. *Geostand Geoenal Res* 44:5–50. <https://doi.org/10.1111/ggr.12313>
- Riley TR, Leat PT, Pankhurst RJ, Harris C (2001) Origins of large volume Rhyolitic Volcanism in the Antarctic Peninsula and Patagonia by Crustal Melting. *J Petrol* 42:1043–1065. <https://doi.org/10.1093/petrology/42.6.1043>
- Rubatto D, Chakraborty S, Dasgupta S (2013) Timescales of crustal melting in the higher himalayan crystallines (Sikkim, Eastern Himalaya) inferred from trace element-constrained monazite and zircon chronology. *Contrib Mineral Petrol* 165:349–372. <https://doi.org/10.1007/s00410-012-0812-y>
- Saxey DW, Reddy SM, Fougereuse D, Rickard WDA (2017) The optimization of zircon analyses by laser-assisted Atom Probe Microscopy: insights from the 91500 zircon Standard. *Microstructural Geochronology: Planet Records Down Atom Scale* 232:293–313. <https://doi.org/10.1002/9781119227250.ch14>
- Saxey DW, Moser DE, Piazzolo S, Reddy SM, Valley JW (2018) Atomic worlds: current state and future of atom probe tomography in geoscience. *Scripta Mater* 148:115–121. <https://doi.org/10.1016/j.scriptamat.2017.11.014>
- Seitz S, Pultitz B, Baumgartner LP, Bouvier A-S (2018) The role of crustal melting in the formation of rhyolites: constraints from SIMS oxygen isotope data (Chon Aike Province, Patagonia, Argentina). *Am Mineral* 103:2011–2027. <https://doi.org/10.2138/am-2018-6520>
- Shannon RD (1976) Revised effective ionic radii and systematic studies of interatomic distances in halides and chalcogenides. *Acta Crystallogr* 32:751–767. <https://doi.org/10.1107/S0567739476001551>
- Smith VG, Tiller WA, Rutter JW (1955) A mathematical analysis of solute redistribution during solidification. *Can J Phys* 33:723–744. <https://doi.org/10.1139/p55-089>
- Szymanowski D, Forni F, Wolff JA, Ellis BS (2020) Modulation of zircon solubility by crystal-melt dynamics. *Geology* 48. <https://doi.org/10.1130/G47405.1>
- Taylor RJM, Reddy SM, Saxey DW, Rickard WDA, Tang F, Borlina CS, Fu RR, Weiss BP, Bagot P, Williams HM, Harrison RJ (2023) Direct age constraints on the magnetism of Jack Hills Zircon. *Sci Adv* 9. <https://doi.org/10.1126/sciadv.add1511>
- Trail D, Thomas JB, Watson EB (2011) The incorporation of hydroxyl into zircon. *Am Mineral* 96:60–67. <https://doi.org/10.2138/am.2011.3506>

- Trail D, Cherniak DJ, Watson EB, Harrison TM, Wiss BP, Szumila I (2016) Li zoning in zircon as a potential geospeedometer and peak temperature indicator. *Contrib Mineral Petrol* 171:25. <https://doi.org/10.1007/s00410-016-1238-8>
- Trail D, Tailby N, Wang Y, Harrison TM, Boehnke P (2017) Aluminum in zircon as evidence for peraluminous and metaluminous melts from the Hadean to present. *Geochim Geophys Geosyst* 18. <https://doi.org/10.1002/2016GC006794>
- Ushikubo T, Kita NK, Cavosie AJ, Wilde SA, Rudnick RL, Valley JW (2008) Lithium in Jack Hills zircons: evidence for extreme weathering of earth's earliest crust. *Earth Planet Sci Lett* 272:666–676. <https://doi.org/10.1016/j.epsl.2008.05.032>
- Valley JW, Cavosie AJ, Ushikubo T, Reinhard DA, Lawrence DF, Larson DJ, Clifton PH, Kelly TF, Wilde SA, Moser DE, Spicuzza MJ (2014) Hadean age for a post-magma-ocean zircon confirmed by atom-probe tomography. *Nat Geosci* 7:219–223. <https://doi.org/10.1038/ngeo2075>
- Valley JW, Reinhard DA, Cavosie AJ, Ushikubo T, Lawrence DF, Larson DJ, Kelly TF, Snoeyenbos DR, Strickland A (2015) Nano- and micro-geochronology in Hadean and Archean zircons by atom-probe tomography and SIMS: New tools for old minerals. *Am Mineral* 100:1355–1377. <https://doi.org/10.2138/am-2015-5134>
- Vavra G (1990) On the kinematics of zircon growth and its petrogenetic significance: a cathodoluminescence study. *Contrib Mineral Petrol* 106:90–99. <https://doi.org/10.1007/BF00306410>
- Wang Y, Trail D (2019) Aluminum partitioning between zircon and haplogranitic melts: the influence of temperature and melt composition. *Chem Geol* 511:71–80. <https://doi.org/10.1016/j.chemgeo.2019.02.016>
- Wang Y, Trail D (2022) Experimental partitioning of Li between zircon and different silicate melts: implications for Li contents in the Hadean and modern crust. *Contrib Miner Petrol* 177:15. <https://doi.org/10.1007/s00410-021-01877-3>
- Watson EB (1996a) Surface enrichment and trace-element uptake during crystal growth. *Geochim Cosmochim Acta* 60:5013–5020. [https://doi.org/10.1016/S0016-7037\(96\)00299-2](https://doi.org/10.1016/S0016-7037(96)00299-2)
- Watson EB (1996b) Dissolution, growth and survival of zircons during crustal fusion: kinetic principles, geological models and implications for isotopic inheritance. *Trans Royal Soc Edinburg: Earth Sci* 87:43–56. <https://doi.org/10.1130/0-8137-2315-9.43>
- Watson EB, Harrison TM (1983) Zircon saturation revisited: temperature and composition effects in a variety of crustal magma types. *Earth Planet Sci Lett* 64:295–304. [https://doi.org/10.1016/0012-821X\(83\)90211-X](https://doi.org/10.1016/0012-821X(83)90211-X)
- Watson EB, Liang Y (1995) A simple model for sector zoning in slowly grown crystals: implications for growth rate and lattice diffusion, with emphasis on accessory minerals in crustal rocks. *Am Mineral* 80:1179–1187. <https://doi.org/10.2138/am-1995-11-1209>
- Watson EB, Müller T (2009) Non-equilibrium isotopic and elemental fractionation during diffusion-controlled crystal growth under static and dynamic conditions. *Chem Geol* 267:111–124. <https://doi.org/10.1016/j.chemgeo.2008.10.036>
- Zhu Z, Campbell IH, Allen CM, Burnham AD (2020) S-type granites: their origin and distribution through time as determined from detrital zircons. *Earth Planet Sci Lett* 536:116140. <https://doi.org/10.1016/j.epsl.2020.116140>

Publisher's note Springer Nature remains neutral with regard to jurisdictional claims in published maps and institutional affiliations.